Check for updates

GEOPHYSICS®

High-resolution reservoir characterization using deep learning aided elastic full-waveform inversion: The North Sea field data example

Journal:	*Geophysics*
Manuscript ID	GEO-2019-0340.R2
Manuscript Type:	Machine Learning and data analytics for geoscience applications
Keywords:	artificial intelligence, full-waveform inversion, North Sea, reservoir characterization, VTI
Area of Expertise:	Anisotropy, Seismic Inversion

SCHOLARONE™
Manuscripts

Downloaded 02/12/20 to 109.171.137.210. Redistribution subject to SEG license or copyright; see Terms of Use at http://library.seg.org/

This paper presented here as accepted for publication in Geophysics prior to copyediting and composition.
© 2020 Society of Exploration Geophysicists.

Downloaded 02/12/20 to 109.171.137.210. Redistribution subject to SEG license or copyright; see Terms of Use at http://library.seg.org/

High-resolution reservoir characterization using deep learning aided elastic full-waveform inversion: The North Sea field data example

Zhen-dong Zhang[1] and Tariq Alkhalifah[1]

1 Department of Physical Science and Engineering,

King Abdullah University of Science and Technology,

Thuwal 23955-6900, Saudi Arabia.

Email: zhendong.zhang@kaust.edu.sa

(January 15, 2020)

Running head: **MLeFWI**

This paper presented here as accepted for publication in Geophysics prior to copyediting and composition.
© 2020 Society of Exploration Geophysicists.

Downloaded 02/12/20 to 109.171.137.210. Redistribution subject to SEG license or copyright; see Terms of Use at http://library.seg.org/

ABSTRACT

Reservoir characterization is an essential component of oil and gas production, as well as exploration. Classic reservoir characterization algorithms, both deterministic and stochastic, are typically based on stacked images and rely on simplifications and approximations to the subsurface (e.g., assuming linearized reflection coefficients). Elastic full-waveform inversion, which aims to match the waveforms of pre-stack seismic data, potentially provides more accurate high-resolution reservoir characterization from seismic data. However, full-waveform inversion can easily fail to characterize deep-buried reservoirs due to illumination limitations. We present a deep learning aided elastic full-waveform inversion strategy using observed seismic data and available well logs in the target area. Five facies are extracted from the well and then connected to the inverted P- and S-wave velocities using trained neural networks, which correspond to the subsurface facies distribution. Such a distribution is further converted to the desired reservoir-related parameters such as velocities and anisotropy parameters using a weighted summation. Finally, we update these estimated parameters by matching the resulting simulated wavefields to the observed seismic data, which corresponds to another round of elastic full-waveform inversion aided by the a priori knowledge gained from the predictions of machine learning. A North Sea field data example, the Volve Oil Field data set, indicates that the use of facies as prior helps resolve the deep-buried reservoir target better than the use of only seismic data.

Keywords: Deep learning, Elastic, VTI, Inversion.

This paper presented here as accepted for publication in Geophysics prior to copyediting and composition.
© 2020 Society of Exploration Geophysicists.

Downloaded 02/12/20 to 109.171.137.210. Redistribution subject to SEG license or copyright; see Terms of Use at http://library.seg.org/

INTRODUCTION

A reservoir is defined as a subsurface body of rock having sufficient porosity and permeability to store and transmit fluids. It is a critical component of a complete petroleum system, and thus, its high-resolution characterization is one of the main objectives of geophysical surveys. The majority of seismic methods, currently used for reservoir characterization are interpretation-based approaches (Partyka et al., 1999; Zhang et al., 2019). Seismic attributes, extracted from stacked images or pre-stack seismic data, are often converted to reservoir-related properties such as a fluid identifier or facies (Chopra and Marfurt, 2007). Extracting seismic attributes from migrated images is an easily-solvable linear inversion, but it requires true-amplitude imaging, which is also challenging in practice. The stochastic reservoir characterization, which aims to match the pre-stack seismic data, requires a reduction in the dimension of seismic attributes for affordable computation (Eidsvik et al., 2004).

An alternative high-resolution reservoir characterization approach is to estimate the reservoir-related properties by matching the resulting simulated waveforms to the observed seismic ones. Elastic full-waveform inversion (FWI) has been used for fractured reservoir characterization in ideal scenarios, in which the background models were known (Zhang et al., 2017). The effective parameters such as the weaknesses or the orientations of fractures can be estimated by matching the waveforms of pre-stack seismic data. Such a waveform inversion strategy faces two main obstacles in solving practical problems (Virieux and Operto, 2009; Yang et al., 2013; Hu et al., 2018): (1) simulated waveforms are often not close to the observed ones due to the incomplete physics used in the simulation; and (2) crosstalk or leakage between different model parameters. Wave equations, either in an acoustic or

This paper presented here as accepted for publication in Geophysics prior to copyediting and composition.
© 2020 Society of Exploration Geophysicists.

Downloaded 02/12/20 to 109.171.137.210. Redistribution subject to SEG license or copyright; see Terms of Use at http://library.seg.org/

even an elastic approximation, can mainly provide accurate traveltime/phase information, but often fails to accurately represent the amplitudes due to the incomplete physics. Seismic anisotropy often ignored to simplify data processing, can have a significant influence on seismic data (Tsvankin et al., 2010). The elimination of crosstalk between multiple parameters can be partially achieved by choosing an optimal parameterization (Operto et al., 2013; Alkhalifah and Plessix, 2014; Alkhalifah, 2016; Zhang and Alkhalifah, 2017; Guitton and Alkhalifah, 2017). Meanwhile, a relatively large offset/depth ratio is needed to separate the contributions from different parameters (scattering angle dependency, Alkhalifah (2014)). Limited by the acquisition spread and the decay of signals at the far-offsets, not all the anisotropy parameters especially at the reservoir depth can be retrieved from surface-collected seismic data. For example, the Thomson parameter ϵ acts as mainly an absorber of the inaccurate amplitudes due, for example, to ignoring density in the parameterization of v_h, v_s, ϵ and η (Guitton and Alkhalifah, 2017). The interpretation of seismic data on their own will provide incomplete information due to the non-uniqueness and the limited spatial resolution. However, additional measurements that may illuminate the reservoir with additional coverage and resolution can provide considerable value (Hu et al., 2009; Li et al., 2017).

A facies-constrained elastic full-waveform inversion strategy can effectively reduce the crosstalk between different parameters by incorporating known facies (Zhang et al., 2018b). Facies, defined as groups of seismic properties and conformity layers that share a particular relationship with geological and lithological properties, can be obtained from wells, sedimentary histories or other investigations (Kemper and Gunning, 2014). Estimated models from surface seismic data and those extracted facies from other geophysical surveys, like well logs, are often measured at very different scales and there are no explicit formulas to

This paper presented here as accepted for publication in Geophysics prior to copyediting and composition.
© 2020 Society of Exploration Geophysicists.

Downloaded 02/12/20 to 109.171.137.210. Redistribution subject to SEG license or copyright; see Terms of Use at http://library.seg.org/

handle the variation in scales. Previously, a Bayesian-based inversion was used to connect the different information in a statistical matter (Zhang et al., 2018b). However, recently emerging machine learning algorithms can do a better job in finding statistical relationships between different types of data (Guitton, 2018; AlRegib et al., 2018; Di et al., 2018; Wu et al., 2019; Zhang and Alkhalifah, 2019). In our proposed approach, we train deep neural networks (DNNs) to build the connection between the estimated models from seismic data and the known facies. In this way, a list of facies is mapped on to a 2D/3D inverted model, which is also known as the facies distribution. The facies distribution can be converted to desired parameters such as velocities and anisotropy parameters. We then use the converted model parameters as a priori for another round of elastic FWI.

In this paper, we start by using a correlation-based elastic FWI to obtain v_p and v_s. Then we calibrate the measured depth of one nearby well using the checkshot information and extract a list of facies from the well. The anisotropy parameters, ϵ and η, are calculated using Backus averaging. Three vertical profiles of estimated v_p, v_s and the corresponding facies are selected as input data features and labels for the deep neural networks, respectively. The trained DNNs are used to estimate the facies distribution. Finally, we convert the distribution to their respective (from the well) parameterization in terms of v_h, v_s, ϵ and η and conduct another round of elastic FWI. A hierarchical anisotropy inversion using the estimated v_p and v_s as input is added for comparison. A two-component ocean-bottom-cable (OBC) data from the North Sea is used to evaluate the proposed method.

This paper presented here as accepted for publication in Geophysics prior to copyediting and composition.
© 2020 Society of Exploration Geophysicists.

Downloaded 02/12/20 to 109.171.137.210. Redistribution subject to SEG license or copyright; see Terms of Use at http://library.seg.org/

CORRELATION BASED ELASTIC FWI

To avoid the often unreliable amplitudes, we use the global correlation as our objective function (Choi and Alkhalifah, 2012), which is given by

$$J_d(\mathbf{m}^i) = -\sum_s \sum_r \widehat{\mathbf{u}} \cdot \widehat{\mathbf{d}}, \tag{1}$$

where $\widehat{\mathbf{u}} = \frac{\mathbf{u}}{||\mathbf{u}||}$ and $\widehat{\mathbf{d}} = \frac{\mathbf{d}}{||\mathbf{d}||}$ are normalized predicted and observed data, respectively. J_d is the corresponding data misfit for the model $\mathbf{m}^i$. The indexes s and r correspond to the source and receiver locations, respectively.

The inverse problem is solved using the first-order elastic wave equation (Vigh et al., 2014), which is given by

$$\begin{pmatrix} \rho \mathbf{I}_3 & 0 \\ 0 & \mathbf{C}^{-1} \end{pmatrix} \frac{\partial \Psi(\mathbf{x},t)}{\partial t} - \begin{pmatrix} 0 & E^T \\ E & 0 \end{pmatrix} \Psi(\mathbf{x},t) - \mathbf{f}(\mathbf{x}_s,t) = 0, \tag{2}$$

where $\Psi(\mathbf{x},t) = (v_1, v_2, v_3, \sigma_1, \sigma_2, \sigma_3, \sigma_4, \sigma_5, \sigma_6)^T$ is a vector containing three particle velocities and six stresses, $\mathbf{I}_3$ is a 3x3 identity matrix. $\mathbf{C}$ is the stiffness matrix, E denotes spatial differentiation, and $\mathbf{f}(\mathbf{x}_s,t)$ is the source, located at $\mathbf{x}_s$.

To obtain the gradient function of the proposed objective function, we take its derivative with respect to the model parameters as follows (Zhang et al., 2018a)

$$\frac{\partial J_d}{\partial \mathbf{m}} = \sum_s \sum_r \frac{\partial \mathbf{u}}{\partial \mathbf{m}} \cdot \left(\frac{1}{||\mathbf{u}||} \left(\widehat{\mathbf{u}} \left(\widehat{\mathbf{u}} \cdot \widehat{\mathbf{d}} \right) - \widehat{\mathbf{d}} \right) \right). \tag{3}$$

For the parameterization of C_{ij}, the Fréchet derivative, $\frac{\partial u(C_{ij},x,t)}{\partial C_{ij}}$, is given by Vigh et al. (2014):

This paper presented here as accepted for publication in Geophysics prior to copyediting and composition.
© 2020 Society of Exploration Geophysicists.

Downloaded 02/12/20 to 109.171.137.210. Redistribution subject to SEG license or copyright; see Terms of Use at http://library.seg.org/

$$\frac{\partial u(C_{ij},s,x,t)}{\partial C_{ij}} = \left(\mathbf{C}^{-T}\frac{\partial C}{\partial C_{ij}}\mathbf{C}^{-1}\left(\frac{\partial \sigma}{\partial t}-\mathbf{f}\right)\right)^{T}_{i=1,...6;j=i,...,6} and \left(\frac{\partial C}{\partial C_{ij}}\right)_{pq} = \begin{cases} 1, p=i, q=j \\ 1, p=j, q=i \\ 0, otherwise \end{cases}, \tag{4}$$

where σ denotes the stress component of the forward-propagated wavefield. $\frac{\partial C}{\partial C_{ij}}$ is a six-by-six matrix with elements defined in equation 4. Here we use the parameterization of C_{ij}, but the gradients for other parameters such as v_p and v_s can be derived using the chain rule. The model is updated iteratively using the l-BFGS method (Liu and Nocedal, 1989), which is written as

$$\mathbf{m} = \mathbf{m}_0 - \alpha \mathbf{H}^{-1}\mathbf{g}, \tag{5}$$

where α is the step length calculated by a standard line-search method, and $\mathbf{H}$ is the approximated Hessian matrix. $\mathbf{m}_0$ and $\mathbf{g}$ are vectors of current model and gradient, respectively.

DEEP NEURAL NETWORKS

A deep neural network as indicated by its name has multiple hidden layers between the input and output layers. It is nothing but a nonlinear system of equations that maps the input into the output. With the input layer denoted as $\mathbf{x}$, the kth hidden layer can be expressed as $\mathbf{a}_k = \phi_k\{\mathbf{W}_k(\ ...\ \phi_1[\mathbf{W}_1\mathbf{x}+\mathbf{b}_1])\ ...\ +\mathbf{b}_k\}$, and the output layer is written as $\mathbf{y} = \mathbf{W}_{l+1}\mathbf{a}_l + \mathbf{b}_{l+1}$, where l denotes the last hidden layer. The input, $\mathbf{x}$, can be raw data or derived data features (e.g., v_s/v_p). The output, $\mathbf{y}$, depends on the problem. For example, it can be integers for classification problems. The data moves in one direction, from the input layer, through the hidden layers and to the output layer in a feedforward fashion. In

This paper presented here as accepted for publication in Geophysics prior to copyediting and composition.
© 2020 Society of Exploration Geophysicists.

Downloaded 02/12/20 to 109.171.137.210. Redistribution subject to SEG license or copyright; see Terms of Use at http://library.seg.org/

each hidden layer, ϕ denotes the activation function, which defines the output of that node with a fed input. The activation function can be the sigmoid, rectified linear unit (ReLu) or some other functions. The training process updates $\mathbf{W}$ and $\mathbf{b}$ for each layer to seek a more accurate mathematical manipulation capable of mapping the input to the output using a loss function of sparse softmax cross entropy (Glorot et al., 2011). Our designed DNNs use three features, v_p, v_s and v_s/v_p, and classified facies as inputs for the training, which are from the conventionally inverted models and the well logs, respectively. Four hidden layers with 256 nodes in each layer are deployed as shown in Figure 1. A ReLu activation function is used (Nair and Hinton, 2010). For each layer, we use a random dropout of 10% to avoid overfitting (Srivastava et al., 2014). Besides, a random data augmentation is applied to balance the proportion of different facies in training the data (Krizhevsky et al., 2017). A total of 2158 training data and 704 test data are used in the training and validation of the network, respectively. A batch size of 128 and 10000 total training steps helped us invert for the network parameters. The Adam gradient is used to update the weighting matrix of neural networks. In our application, we output the probabilities for all facies instead of one specific kind. After obtaining the percentages of being a certain facies, we can calculate the subsurface facies distribution (converted to v_h, v_s, ϵ and η) by a weighted summation over n_f facies, $m^p = \sum_{i=1}^{n_f} p_i m_i$. m^p denotes averaged P-, S-wave velocities or anisotropy parameters, which is equivalent to the posterior expectation in Zhang et al. (2018b). p_i and m_i are probabilities estimated by the trained DNNs and the known facies, respectively. Such a weighted summation avoids potential bias caused by a particular kind of facies when the DNNs fail. Besides, it can be used to interpolate between different facies. In practice, we can never know all the facies in the subsurface and we do not need to know all of them in our proposed method. The probabilities act as interpolation weights for the known facies.

This paper presented here as accepted for publication in Geophysics prior to copyediting and composition.
© 2020 Society of Exploration Geophysicists.

Downloaded 02/12/20 to 109.171.137.210. Redistribution subject to SEG license or copyright; see Terms of Use at http://library.seg.org/

If the corresponding facies for certain pairs of v_p and v_s is not available as prior knowledge, the averaged parameters still have a chance of being (or close to) the correct ones through interpolation.

FACIES CONSTRAINTS

In a previous study (Zhang et al., 2018b), the facies distribution is converted to desired parameters used in inversion, which are then used as model constraints. The process can be expressed as

$$J_{reg}(\mathbf{m}^i) = J_d(\mathbf{m}^i) + \beta||\mathbf{m}^i - \mathbf{m}^p||^2, \tag{6}$$

where $J_d(\mathbf{m}^i)$ measures the data mismatch (equation 1), $\mathbf{m}^i$ and $\mathbf{m}^p$ denote the inverted and prior models, respectively. β balances the amount of seismic data matching and utilizing the known facies in this case. The choice of β is case dependent. Mathematically, it can be determined by the L-curve method (Hansen and OLeary, 1993). However, in practice, seismic data can be very noisy for land acquisition and we may use a relatively large β, which means the extracted facies are trusted more in inversion. For high-quality seismic data, such as marine data, we might choose a relatively small β to assign a larger weight to seismic-data matching.

Seismic facies can be obtained from different sources such as well logs, core analysis and sedimentation history. Here, we extract a list of facies from the P- and S-wave velocity well log as shown in Figure 2. The reservoir is located at 2.75-3.12 km depth, with an overlying seal rock. The well log covers the depth around the reservoir layer and the well is slightly deviated. We calibrate the depth of the top and bottom of the dominant layers using the checkshot (red line). Five facies are extracted from the reservoir area by manually grouping

This paper presented here as accepted for publication in Geophysics prior to copyediting and composition.
© 2020 Society of Exploration Geophysicists.

Downloaded 02/12/20 to 109.171.137.210. Redistribution subject to SEG license or copyright; see Terms of Use at http://library.seg.org/

the velocities. We only extract the dominant facies in the target area. More experienced interpreters can utilize more advanced classifications of facies and include more desirable model parameters, i.e., porosity and fluid identifier. The interpreted facies are used as labels in supervised learning. We then calculate the anisotropy parameters ϵ and η using Backus averaging (Berryman et al., 1999) as shown in Figure 3 to upscale the sonic well velocities. The delineated facies have different combinations in terms of v_p, v_s, ϵ and η as listed in Table 1. The listed parameter values are the averaged values within the facies. The seal rock has a strong anisotropy, while the reservoir layer is almost isotropic.

The DNN takes inverted v_p, v_s and v_s/v_p as input; the facies list is then mapped to the output of DNN, which is the spatial distribution of facies, and result in the estimated model parameters. The estimated facies distribution might include errors at the early stages of the inversion and can be improved by matching the observed seismic data in another scenario of FWI. The workflow of the proposed method is summarized in Figure 4. We first obtain the initial estimates for v_p and v_s using elastic FWI and a list of known facies in the target area. Then we train the deep neural networks to map the known facies to the initially estimated v_p and v_s and obtain the distribution of any desired models (v_p, v_s, ϵ and η in our case). Finally, we use the smoothed version of such models as an input model for another round of elastic FWI. We can update the facies distribution and models iteratively by applying multiple nested inversions.

NUMERICAL EXAMPLE

We apply the proposed inversion strategy to a 2D line of the Volve data set. The seal layer and the reservoir, located at 2.75-3.12 km depth, are the main imaging goals. We use the raw data set with limited processing applied that includes polarity correction, instrumental

This paper presented here as accepted for publication in Geophysics prior to copyediting and composition.
© 2020 Society of Exploration Geophysicists.

Downloaded 02/12/20 to 109.171.137.210. Redistribution subject to SEG license or copyright; see Terms of Use at http://library.seg.org/

deconvolution and data quality control. For the inversion, we use 240 shots and 240 two-component receivers distributed evenly at 50 m and 25 m, respectively. The length of the ocean-bottom cable (OBC) is 6 km and the sources are evenly distributed along a 12 km line just below the sea surface. A modified free-surface boundary condition, which can suppress strong surface waves, is used in the simulation (He et al., 2016). We convolve the observed data with the half-order differentiation of the known wavelet, and thus, we avoid source estimation, while correcting the phase discrepancy between the 3D acquisition and the 2D simulation (Pica et al., 1990; Yoon et al., 2012). The initial model is a 1D smoothed version of the model provided by the data owners, and shown in Figure 5. Only one frequency band (2-12 Hz) is used for the inversion. We first conduct an isotropic elastic FWI using the primary arrivals to improve the 1D initial model (not shown here) and then we use the full data to refine the inverted isotropic model as shown in Figure 6. We apply a hierarchical vertical transverse isotropic (VTI) inversion (Oh and Alkhalifah, 2018), in which we use the parameterization v_h, v_s, ϵ and η as shown in Figure 7. The high-velocity seal and the relatively low-velocity layer appear in the inverted results. Finally, we train deep neural networks to build the connection between the estimated v_p and v_s (Figure 6) and the extracted facies (Table 1). As mentioned above, we use a four-layer deep neural network and each layer has 256 nodes with a 10% random dropout. The input features are v_p, v_s and v_s/v_p and the outputs are probabilities of being one of the known facies. We use three vertical profiles from the estimated v_p and v_s (Figure 6) to generate the training data set. The three lines are located at X=4.5, 6.0 and 7.5 km to cover possible illumination variations. The selection of such a training set should consider the diversity of inversion patterns (structure and illumination variations) and include as much as possible unique patterns (i.e., facies) for efficient training. A vertical line located at X=6.75 km is used

This paper presented here as accepted for publication in Geophysics prior to copyediting and composition.
© 2020 Society of Exploration Geophysicists.

Downloaded 02/12/20 to 109.171.137.210. Redistribution subject to SEG license or copyright; see Terms of Use at http://library.seg.org/

to generate the test data set. The training loss and the test accuracy history after every 100 steps are plotted in Figure 8. The training set accuracy is about 0.9, while the test set accuracy stays around 0.7. This often indicates that the training data are not over-fitted. After training, we use all the model pixels to estimate the subsurface facies distribution. The distribution is further converted to v_h, v_s, ϵ and η using the proposed weighted summation, shown in Figure 9. We slightly smooth the converted model (below 2.5 km) and merge it into the model from the VTI inversion (above 2.5 km) and generate a new initial model for another VTI inversion. The updated model is shown in Figure 10. The high-velocity seal rock with a strong anisotropy above a low-velocity zone is improved. Also, our proposed inversion managed to obtain a high-resolution ϵ and a lower-resolution η at the reservoir depth, which was guided by the data. Usually, η in the deeply buried seal rocks is not recoverable from the seismic data with limited offsets since it requires a relatively large offset/depth ratio (Alkhalifah and Plessix, 2014). The interleaved predicated and observed vertical- and horizontal-component data plot (Figure 11) of the initial model indicates that the initial model can provide reasonably good prediction in the near offsets. The inversion considering isotropic elasticity helps to match the data in the far offsets and recovers some dominant reflections as shown in Figure 12. The interleaved data comparisons indicate that adding anisotropy effects can help us obtain simulated data that match the observed data even better (Figures 12 and 13). The deep learning aided approach can help improve the matching of deep reflections (Figures 13 and 14). A zoomed-in view of the marked area is shown in Figure 15. We can find the improvements in phase matching marked by the arrows. We plot the data-matching history for the different inversion scenarios as shown in Figure 16. It shows that the isotropic inversion reduces the data misfit by 40% and the follow-up deep learning aided inversion can further reduce the data misfit by about an

This paper presented here as accepted for publication in Geophysics prior to copyediting and composition.
© 2020 Society of Exploration Geophysicists.

Downloaded 02/12/20 to 109.171.137.210. Redistribution subject to SEG license or copyright; see Terms of Use at http://library.seg.org/

additional 5%. The data mismatch suddenly increases after adding facies constraints, but it reduces to the same level as the hierarchical VTI inversion after few iterations of inversion. The inversion stops when the updates cannot satisfy the Wolfe line-search condition (Wolfe, 1969). The facies distribution was estimated once in this example. We also compare the inverted vertical P-wave velocities with the one from the checkshot nearby in Figure 17. The isotropic elastic FWI seems to be able to improve the initial model but with a low-resolution. There are some further improvements after considering the anisotropic effects but the improvements are still mild unless the facies information are used as constraints. The estimated vertical P-wave velocity using the proposed approach is close to the one from the checkshot in the target depth. Remarkably, we did not use well logs or checkshots as direct model constraints in the proposed inversion. Also, we were given an inverted VTI model as shown in Figure 18, which was obtained using a layer-stripping tomography approach. To plot our inverted and their reference models using the same color scale, we clip the high values of v_h and v_s in Figure 18. A vertical-profile comparison of the parameters in terms of v_h, v_s, ϵ and η between the proposed inversion and the provided reference model is shown in Figure 19. The facies constraints are only applied around the reservoir area (below 2.3 km depth), where the well logs are available. The horizontal velocities (v_h) have a reasonable match with those predicted by the data providers. There is a depth mismatch due to the lack of background ϵ information. The inverted v_s does not match the reference model well without the facies constraints (e.g., the shallow area), which might be caused by the ignorance of S-wave anisotropy. For the deep area with facies constraints, the inverted v_s is closer to the reference model. Otherwise, the inverted v_s might have crosstalks with v_p due to the limited scattering angles. The inverted ϵ has high resolution and it often acts as an absorber of phenomena not addressed in our approximation, like

This paper presented here as accepted for publication in Geophysics prior to copyediting and composition.
© 2020 Society of Exploration Geophysicists.

Downloaded 02/12/20 to 109.171.137.210. Redistribution subject to SEG license or copyright; see Terms of Use at http://library.seg.org/

density variations (Guitton and Alkhalifah, 2017). The inverted anisotropy parameters are closer to those derived using Backus averaging (Figure 3), which have a discrepancy with the reference model. We use the provided tomographic based, and well assisted, model to provide an opportunity to assess our results. We do not expect, what we refer to them as, a reference model to exactly represent the Earth, as they are vulnerable to their own limited assumptions of the Earth. In our inverted results, we obtain large η in the shallow part, and though they are not part of the region covered by the well information, the eta inversion, considering the large offset to depth ratio in the shallow part, might be accurate. The matching of the moveout at the far offset also seems to support that.

DISCUSSION

We use deep neural networks to classify the initially inverted elastic model using three inputs, the inverted v_p, v_s and v_s/v_p at the wells. The classification in terms of facies are used to map the facies information, which may include even anisotropic information from the well, to the rest of the model area. The mapping process is based on a statistically weighted contribution of the facies to every grid point in the model. We use these mapped parameters as an a priori for the next round of anisotropic elastic inversion. The inputs to the neural network can include additional inverted parameters, and even uncertainty information. The additional input information is expected to improve the statistical distribution of the facies. In addition, the identified facies can include additional information extracted from the well, such as the Q factor or orthorhombic anisotropy information. All of which can be used to constrain the inversion considering more complete physics, like an orthorhombic viscoelastic inversion. The structural constraints can enhance the similarity in geometry between v_p, v_s and the anisotropic parameters, which may be also helpful for the mapping in the example.

This paper presented here as accepted for publication in Geophysics prior to copyediting and composition.
© 2020 Society of Exploration Geophysicists.

Downloaded 02/12/20 to 109.171.137.210. Redistribution subject to SEG license or copyright; see Terms of Use at http://library.seg.org/

One of the possible limitations, in this case, is that the actual v_p and v_s may have different structures due to fluid content.

The DNN is expected to learn some aspects of the varying illumination and amplitude characteristics of the inverted model, specifically near the well locations. It may, however, suffer in areas that are not represented by illumination features covered by the well locations, like at edges of the model. A well-behaved elastic or even anisotropic inversion, in terms of illumination distribution, is important to the application of this DNN. DNN learns from what is used as input and output in the training set. If we are missing features in the training set, DNN will find it hard to predict those features. For example, in the area with strong lateral variations, we might need more wells to obtain the needed facies information. The weighted summation might help interpolate the inter-medium values for the missing facies. Also, the extracted list of facies (Table 1) uses the mean values for each model parameter, which has an implicit Gaussian-distribution assumption to the measurements within one facies (Zhang et al., 2018b). For non-Gaussian distributions, we may need to modify the weighted summation to take the actual distribution into consideration. Otherwise, we can use finer layers (more labels) to maintain the Gaussian assumption.

It is known that not all the model parameters are resolvable by only matching the surface-collected seismic data, especially for field data applications. For better characterization of the subsurface, more model parameters are needed, which requires utilizing more data such as well logs as complementary to seismic data. Usually, well logs are available along with seismic data corresponding usually to a target reservoir area. One of the difficulties in utilizing well log data is that seismic data and well logs reflect the Earth at two different scales and there are no explicit equations to connect them. Deep neural networks are capable of building such connections in a statistical sense. The extraction of facies is

This paper presented here as accepted for publication in Geophysics prior to copyediting and composition.
© 2020 Society of Exploration Geophysicists.

Downloaded 02/12/20 to 109.171.137.210. Redistribution subject to SEG license or copyright; see Terms of Use at http://library.seg.org/

not limited to well logs. More experienced interpreters can do this job better in practice. The extraction of facies in a strongly heterogeneous area might be challenging in practice. However, most sedimentary reservoirs have mild lateral structural variations. With limited prior information, we still have a chance to improve the estimation by matching the observed seismic data.

CONCLUSIONS

We develop a framework to invert for a relatively high-resolution anisotropic description of the reservoir by utilizing surface seismic and facies information from a well, and using deep neural networks (DNNs) to connect them statistically. We applied this DNN-assisted elastic full waveform inversion on OBC data from the North Sea and obtained a reasonable inversion of the reservoir region. The comparison with the well information, as well as the reference model provided with the data, reveal the ability of the approach in mapping the well information to the rest of the model space.

ACKNOWLEDGMENTS

We thank Jeffrey Shragge, Weichang Li, Wenyi Hu and two anonymous reviewers, for the effort put into the review of the manuscript. We also want to thank Equinor and the former Volve license partners ExxonMobil E&P Norway AS and Bayerngas Norge AS, for the release of the Volve data. The views expressed in this paper are the views of the authors and do not necessarily reflect the views of Equinor and the former Volve field license partners. For computer time, this research used the resources of the Supercomputing Laboratory at King Abdullah University of Science & Technology (KAUST) in Thuwal, Saudi Arabia.

This paper presented here as accepted for publication in Geophysics prior to copyediting and composition.
© 2020 Society of Exploration Geophysicists.

Downloaded 02/12/20 to 109.171.137.210. Redistribution subject to SEG license or copyright; see Terms of Use at http://library.seg.org/

REFERENCES

Alkhalifah, T., 2014, Scattering-angle based filtering of the waveform inversion gradients: Geophysical Journal International, **200**, no. 1, 363–373.

———, 2016, Research note: Insights into the data dependency on anisotropy: An inversion prospective: Geophysical Prospecting, **64**, no. 2, 505–513.

Alkhalifah, T. and R.-É. Plessix, 2014, A recipe for practical full-waveform inversion in anisotropic media: An analytical parameter resolution study: Geophysics, **79**, no. 3, R91–R101.

AlRegib, G., M. Deriche, Z. Long, H. Di, Z. Wang, Y. Alaudah, M. A. Shafiq, and M. Alfarraj, 2018, Subsurface structure analysis using computational interpretation and learning: A visual signal processing perspective: IEEE Signal Processing Magazine, **35**, no. 2, 82–98.

Berryman, J. G., V. Y. Grechka, and P. A. Berge, 1999, Analysis of Thomsen parameters for finely layered VTI media: Geophysical Prospecting, **47**, no. 6, 959–978.

Choi, Y. and T. Alkhalifah, 2012, Application of multi-source waveform inversion to marine streamer data using the global correlation norm: Geophysical Prospecting, **60**, no. 4, 748–758.

Chopra, S. and K. J. Marfurt, 2007, Seismic attributes for prospect identification and reservoir characterization: Society of Exploration Geophysicists.

Di, H., Z. Wang, and G. AlRegib, 2018, Seismic fault detection from post-stack amplitude by convolutional neural networks: 80th EAGE Conference and Exhibition 2018, Tu D 11, European Association of Geoscientists & Engineers.

Eidsvik, J., P. Avseth, H. Omre, T. Mukerji, and G. Mavko, 2004, Stochastic reservoir characterization using prestack seismic data: Geophysics, **69**, no. 4, 978–993.

This paper presented here as accepted for publication in Geophysics prior to copyediting and composition.
© 2020 Society of Exploration Geophysicists.

Downloaded 02/12/20 to 109.171.137.210. Redistribution subject to SEG license or copyright; see Terms of Use at http://library.seg.org/

Glorot, X., A. Bordes, and Y. Bengio, 2011, Deep sparse rectifier neural networks: Proceedings of the fourteenth international conference on artificial intelligence and statistics, 315–323, JMLR W&CP.

Guitton, A., 2018, 3D convolutional neural networks for fault interpretation: 80th EAGE Conference and Exhibition 2018, TU D 10, European Association of Geoscientists & Engineers.

Guitton, A. and T. Alkhalifah, 2017, A parameterization study for elastic vti full-waveform inversion of hydrophone components: Synthetic and North Sea field data examples: Geophysics, **82**, no. 6, R299–R308.

Hansen, P. C. and D. P. OLeary, 1993, The use of the l-curve in the regularization of discrete ill-posed problems: SIAM Journal on Scientific Computing, **14**, no. 6, 1487–1503.

He, W., R. Plessix, and S. Singh, 2016, Modified boundary conditions for elastic inversion of active land seismic data in VTI media: 78th EAGE Conference and Exhibition 2016, We P1 14, European Association of Geoscientists & Engineers.

Hu, W., A. Abubakar, and T. M. Habashy, 2009, Joint electromagnetic and seismic inversion using structural constraints: Geophysics, **74**, no. 6, R99–R109.

Hu, W., J. Chen, J. Liu, and A. Abubakar, 2018, Retrieving low wavenumber information in FWI: An overview of the cycle-skipping phenomenon and solutions: IEEE Signal Processing Magazine, **35**, no. 2, 132–141.

Kemper, M. and J. Gunning, 2014, Joint impedance and facies inversion–seismic inversion redefined: First Break, **32**, no. 9, 89–95.

Krizhevsky, A., I. Sutskever, and G. E. Hinton, 2017, Imagenet classification with deep convolutional neural networks: Communications of the ACM, **60**, no. 6, 84–90.

Li, W., M. Deffenbaugh, D. G. Gillard, G. Chen, and X. Xu, 2017, Method for estimating

This paper presented here as accepted for publication in Geophysics prior to copyediting and composition.
© 2020 Society of Exploration Geophysicists.

Downloaded 02/12/20 to 109.171.137.210. Redistribution subject to SEG license or copyright; see Terms of Use at http://library.seg.org/

subsurface properties from geophysical survey data using physics-based inversion. (US Patent 9,696,442).

Liu, D. C. and J. Nocedal, 1989, On the limited memory BFGS method for large scale optimization: Mathematical programming, **45**, no. 1-3, 503–528.

Nair, V. and G. E. Hinton, 2010, Rectified linear units improve restricted boltzmann machines: Proceedings of the 27th international conference on machine learning (ICML-10), 807–814.

Oh, J.-W. and T. Alkhalifah, 2018, Optimal full-waveform inversion strategy for marine data in azimuthally rotated elastic orthorhombic media: Geophysics, **83**, no. 4, R307–R320.

Operto, S., Y. Gholami, V. Prieux, A. Ribodetti, R. Brossier, L. Metivier, and J. Virieux, 2013, A guided tour of multiparameter full-waveform inversion with multicomponent data: From theory to practice: The Leading Edge, **32**, no. 9, 1040–1054.

Partyka, G., J. Gridley, and J. Lopez, 1999, Interpretational applications of spectral decomposition in reservoir characterization: The Leading Edge, **18**, no. 3, 353–360.

Pica, A., J. Diet, and A. Tarantola, 1990, Nonlinear inversion of seismic reflection data in a laterally invariant medium: Geophysics, **55**, no. 3, 284–292.

Srivastava, N., G. Hinton, A. Krizhevsky, I. Sutskever, and R. Salakhutdinov, 2014, Dropout: a simple way to prevent neural networks from overfitting: The Journal of Machine Learning Research, **15**, no. 1, 1929–1958.

Tsvankin, I., J. Gaiser, V. Grechka, M. Van Der Baan, and L. Thomsen, 2010, Seismic anisotropy in exploration and reservoir characterization: An overview: Geophysics, **75**, no. 5, A15–A29.

Vigh, D., K. Jiao, D. Watts, and D. Sun, 2014, Elastic full-waveform inversion application using multicomponent measurements of seismic data collection: Geophysics, **79**, no. 2,

This paper presented here as accepted for publication in Geophysics prior to copyediting and composition.
© 2020 Society of Exploration Geophysicists.

Downloaded 02/12/20 to 109.171.137.210. Redistribution subject to SEG license or copyright; see Terms of Use at http://library.seg.org/

R63–R77.

Virieux, J. and S. Operto, 2009, An overview of full-waveform inversion in exploration geophysics: Geophysics, **74**, no. 6, WCC1–WCC26.

Wolfe, P., 1969, Convergence conditions for ascent methods: SIAM Review, **11**, no. 2, 226–235.

Wu, Y., Y. Lin, Z. Zhou, D. C. Bolton, J. Liu, and P. Johnson, 2019, Deepdetect: A cascaded region-based densely connected network for seismic event detection: IEEE Transactions on Geoscience and Remote Sensing, **57**, no. 1, 62–74.

Yang, T., J. Shragge, and P. Sava, 2013, Illumination compensation for image-domain wavefield tomography: Geophysics, **78**, no. 5, U65–U76.

Yoon, K., S. Suh, J. Cai, and B. Wang, 2012, Improvements in time domain FWI and its applications, *in* SEG Technical Program Expanded Abstracts 2012, 1–5, Society of Exploration Geophysicists.

Zhang, T.-F., P. Tilke, E. Dupont, L.-C. Zhu, L. Liang, and W. Bailey, 2019, Generating geologically realistic 3d reservoir facies models using deep learning of sedimentary architecture with generative adversarial networks: Petroleum Science, **16**, 1–9.

Zhang, Z., T. Alkhalifah, J.-W. Oh, and I. Tsvankin, 2017, Estimation of fracture parameters using elastic full-waveform inversion, *in* SEG Technical Program Expanded Abstracts 2017, 3272–3276, Society of Exploration Geophysicists.

Zhang, Z., T. Alkhalifah, Z. Wu, Y. Liu, B. He, and J. Oh, 2018a, Normalized nonzero-lag crosscorrelation elastic full-waveform inversion: Geophysics, **84**, no. 1, R15–R24.

Zhang, Z.-D. and T. Alkhalifah, 2017, Full waveform inversion using oriented time-domain imaging method for vertical transverse isotropic media: Geophysical Prospecting, **65**, no. S1, 166–180.

This paper presented here as accepted for publication in Geophysics prior to copyediting and composition.
© 2020 Society of Exploration Geophysicists.

Downloaded 02/12/20 to 109.171.137.210. Redistribution subject to SEG license or copyright; see Terms of Use at http://library.seg.org/

———, 2019, Regularized elastic full waveform inversion using deep learning: Geophysics, **84**, no. 5, R741–R751.

Zhang, Z.-d., T. Alkhalifah, E. Z. Naeini, and B. Sun, 2018b, Multiparameter elastic full waveform inversion with facies-based constraints: Geophysical Journal International, **213**, no. 3, 2112–2127.

This paper presented here as accepted for publication in Geophysics prior to copyediting and composition.
© 2020 Society of Exploration Geophysicists.

Downloaded 02/12/20 to 109.171.137.210. Redistribution subject to SEG license or copyright; see Terms of Use at http://library.seg.org/

LIST OF TABLES

This paper presented here as accepted for publication in Geophysics prior to copyediting and composition.
© 2020 Society of Exploration Geophysicists.

Downloaded 02/12/20 to 109.171.137.210. Redistribution subject to SEG license or copyright; see Terms of Use at http://library.seg.org/

LIST OF FIGURES

1 The Neural Network architecture. Three features are used in the input layer. Four hidden layers with 256 nodes are fully connected neural networks with a dropout rate of 10%. The output layer provides probabilities of being certain facies for the current input.

2 A depth-calibrated well log and the extracted facies. Five dominant facies are extracted at the target depth.

3 Calculated anisotropy parameters in terms of ϵ and η using Backus averaging. They're used to provide the facies information.

4 The workflow for the proposed inversion method. The facies distribution and the regularly inverted models can be updated, iteratively.

5 The initial 1D models.

6 The inverted models using an isotropic elastic FWI. a) v_p and b) v_s.

7 The inverted models using the anisotropic elastic FWI. a) v_h, b) v_s, c) ϵ and d) η.

8 Normalized training loss at every 100 steps. A total of 90% training loss is achieved with a random dropout of 10% for each layer, while the validation accuracy stays around 70%.

9 The predicted facies distribution after training. They are converted to the parameters of a) v_h, b) v_s, c) ϵ and d) η. The number of colors is not equal to the number of faceis since the weighted summation can generate more parameter values in between and also different faceis can have the same value for certain parameters.

10 The inverted models using the anisotropic elastic FWI with facies constraints. a)

This paper presented here as accepted for publication in Geophysics prior to copyediting and composition.
© 2020 Society of Exploration Geophysicists.

Downloaded 02/12/20 to 109.171.137.210. Redistribution subject to SEG license or copyright; see Terms of Use at http://library.seg.org/

v_h, b) v_s, c) ϵ and d) η.

11 A shot gather displaying interleaved predicted and observed data using the initial v_p and v_s as shown in Figure 5. a) Vertical and b) horizontal components. The dashed rectangular indicates the zoomed-in view plotted in Figure 15.

12 A shot gather displaying interleaved predicted and observed data using the estimated v_p and v_s from isotropic inversion as shown in Figure 6. a) Vertical and b) horizontal components.

13 A shot gather displaying interleaved predicted and observed data using the estimated v_h, v_s, ϵ and η from hierarchic VTI inversion as shown in Figure 7. a) Vertical and b) horizontal components.

14 A shot gather displaying interleaved predicted and observed data using the deep learning aided VTI inversion as shown in Figure 10. The matching of reflections of the vertical component are improved compared to the hierarchical VTI inversion (Figure 13). a) Vertical and b) horizontal components.

15 A zoomed-in view of the vertical-component of the shot gathers. a), b), c) and d) are corresponding to the marked areas in Figures 12, 13, 14 and 16, respectively. The arrows mark the improved phase matching.

16 Data matching history. There are three sequential inversions: 1) isotropic first arrival FWI, 2) isotropic full data FWI and 3) VTI inversions. The VTI inversions are parallel inversions: one is the hierarchical VTI inversion and another one is the proposed machine-learning aided inversion. The isotropic inversion reduces the data misfit by 40% and the follow-up deep learning aided inversion can further reduce the data misfit by about an additional 5%.

This paper presented here as accepted for publication in Geophysics prior to copyediting and composition.
© 2020 Society of Exploration Geophysicists.

Downloaded 02/12/20 to 109.171.137.210. Redistribution subject to SEG license or copyright; see Terms of Use at http://library.seg.org/

17 Vertical P-wave velocity profiles at X=5.25 km.

18 The reference VTI model provided by Equinor. a) v_h, b) v_s, c) ϵ and d) η. They are obtained using the layer-stripping tomography technique.

19 A vertical-profile comparison of the parameters in terms of v_h, v_s, ϵ and η between the proposed inversion and the provided reference model at location X=5.25 km. The facies constraint is only applied below 2.3 km due to the availability of well log data.

This paper presented here as accepted for publication in Geophysics prior to copyediting and composition.
© 2020 Society of Exploration Geophysicists.

Downloaded 02/12/20 to 109.171.137.210. Redistribution subject to SEG license or copyright; see Terms of Use at http://library.seg.org/

Table 1: List of facies in the target area.

	f1	**f2**	**f3**	**f4**	**f5**
v_p	3.45	4.2	4.0	3.1	4.1
v_s	1.7	2.4	2.2	1.5	2.4
ϵ	0.01	0.1	0.0	0.07	0.05
η	0.05	0.3	0.0	0.1	0.1

This paper presented here as accepted for publication in Geophysics prior to copyediting and composition.
© 2020 Society of Exploration Geophysicists.

Downloaded 02/12/20 to 109.171.137.210. Redistribution subject to SEG license or copyright; see Terms of Use at http://library.seg.org/

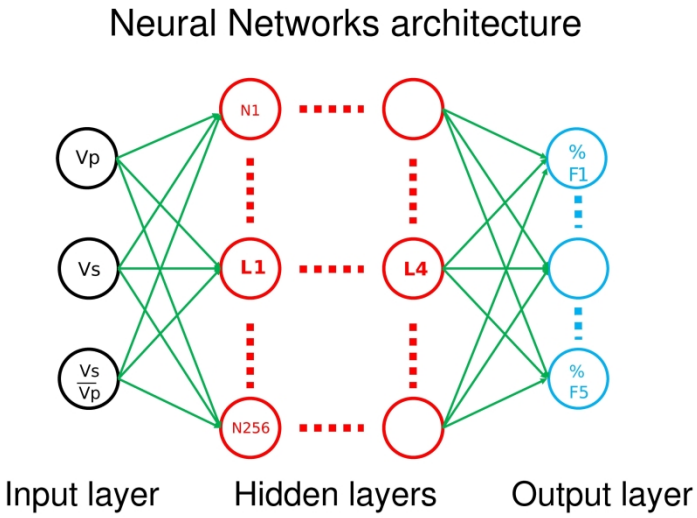

Figure1: The Neural Network architecture. Three features are used in the input layer. Four hidden layers with 256 nodes are fully connected neural networks with a dropout rate of 10%. The output layer provides probabilities of being certain facies for the current input.

338x190mm (300 x 300 DPI)

This paper presented here as accepted for publication in Geophysics prior to copyediting and composition.
© 2020 Society of Exploration Geophysicists.

Downloaded 02/12/20 to 109.171.137.210. Redistribution subject to SEG license or copyright; see Terms of Use at http://library.seg.org/

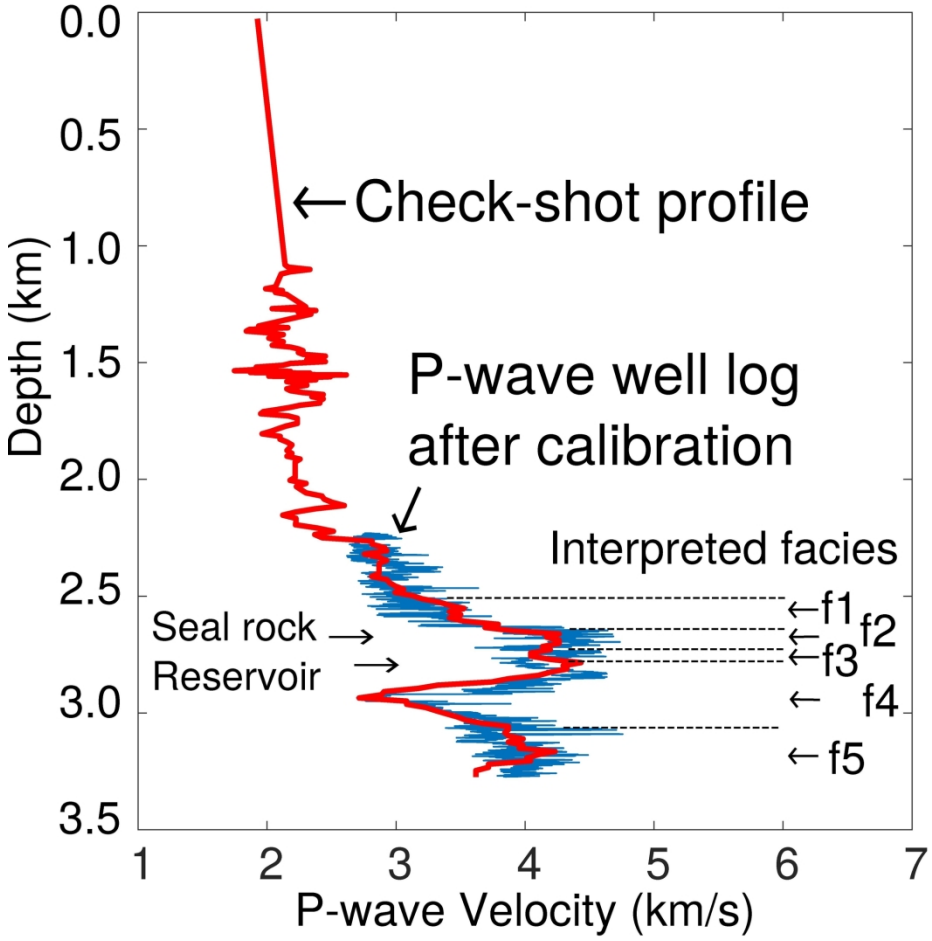

Figure2: A depth-calibrated well log and the extracted facies. Five dominant facies are extracted at the target depth.

199x199mm (300 x 300 DPI)

This paper presented here as accepted for publication in Geophysics prior to copyediting and composition.
© 2020 Society of Exploration Geophysicists.

Downloaded 02/12/20 to 109.171.137.210. Redistribution subject to SEG license or copyright; see Terms of Use at http://library.seg.org/

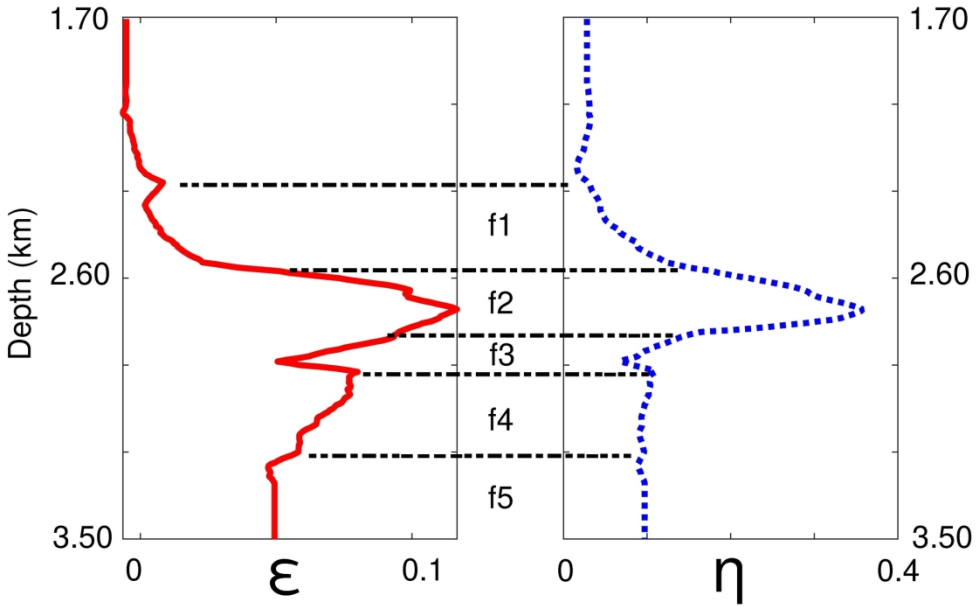

Figure3: Calculated anisotropy parameters in terms of ϵ and η using Backus averaging. They're used to provide the facies information.

181x116mm (300 x 300 DPI)

This paper presented here as accepted for publication in Geophysics prior to copyediting and composition.
© 2020 Society of Exploration Geophysicists.

Downloaded 02/12/20 to 109.171.137.210. Redistribution subject to SEG license or copyright; see Terms of Use at http://library.seg.org/

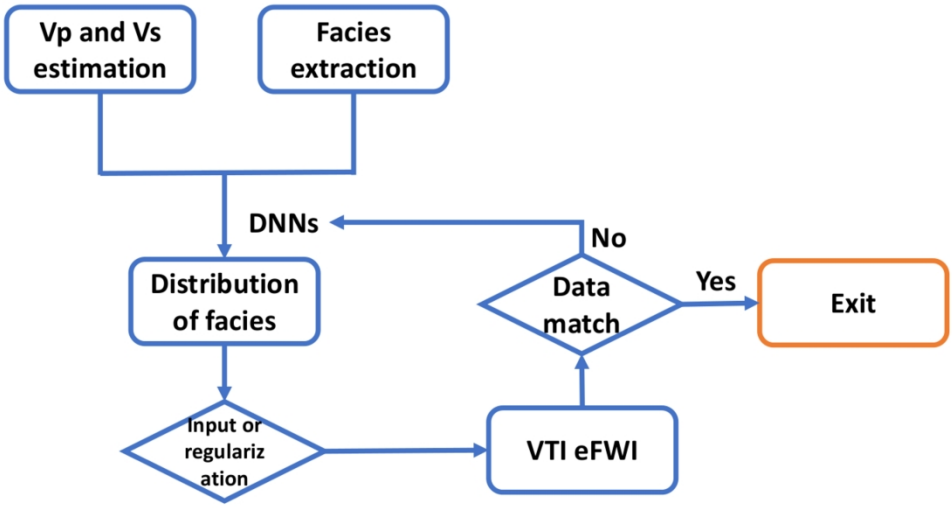

Figure4: The workflow for the proposed inversion method. The facies distribution and the regularly inverted models can be updated, iteratively.

404x222mm (300 x 300 DPI)

This paper presented here as accepted for publication in Geophysics prior to copyediting and composition.
© 2020 Society of Exploration Geophysicists.

Downloaded 02/12/20 to 109.171.137.210. Redistribution subject to SEG license or copyright; see Terms of Use at http://library.seg.org/

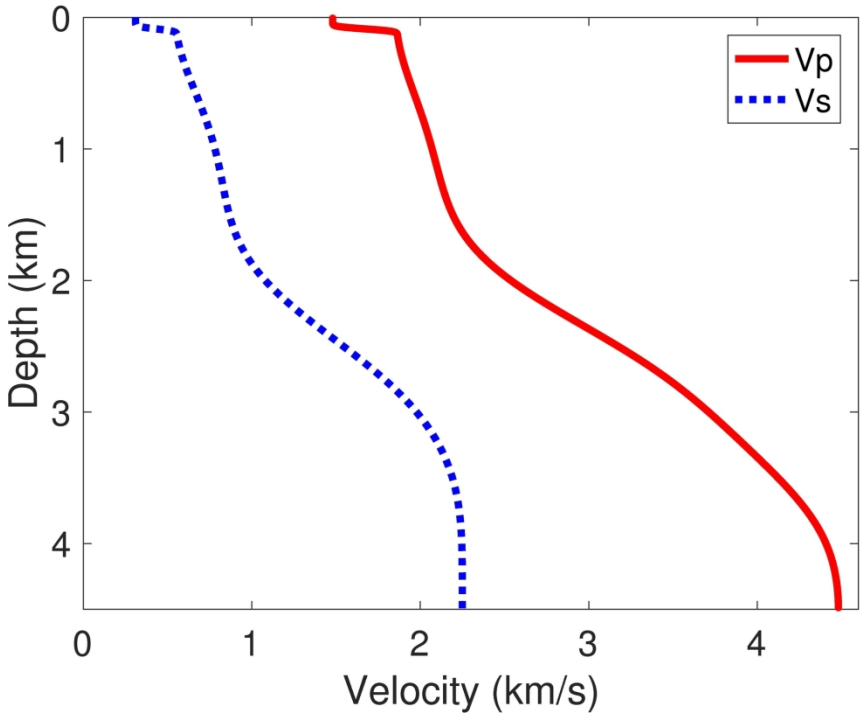

Figure5: The initial 1D models.

197x148mm (300 x 300 DPI)

This paper presented here as accepted for publication in Geophysics prior to copyediting and composition.
© 2020 Society of Exploration Geophysicists.

Downloaded 02/12/20 to 109.171.137.210. Redistribution subject to SEG license or copyright; see Terms of Use at http://library.seg.org/

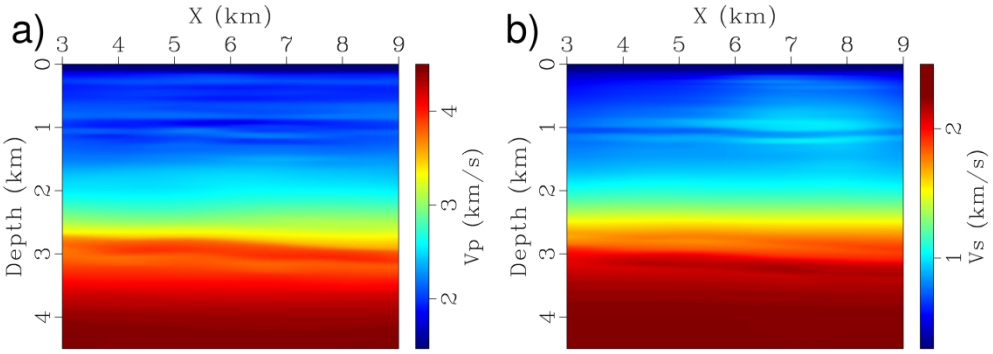

Figure6: The inverted models using an isotropic elastic FWI. a) v_p and b) v_s.

343x123mm (300 x 300 DPI)

This paper presented here as accepted for publication in Geophysics prior to copyediting and composition.
© 2020 Society of Exploration Geophysicists.

Downloaded 02/12/20 to 109.171.137.210. Redistribution subject to SEG license or copyright; see Terms of Use at http://library.seg.org/

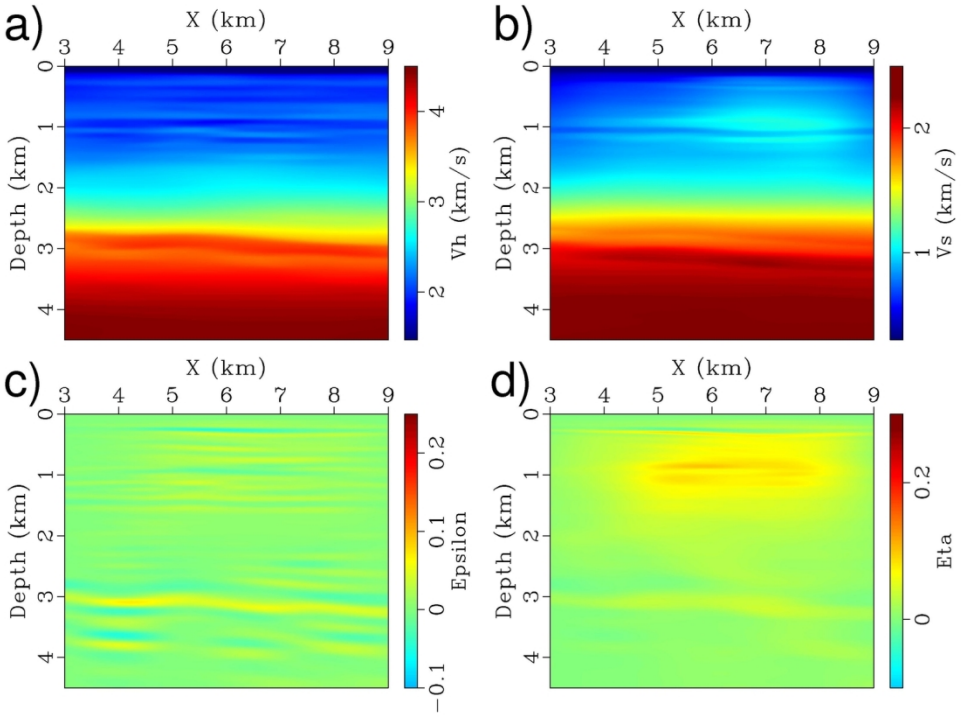

Figure7: The inverted models using the anisotropic elastic FWI. a) v_h, b) v_s, c) ϵ and d) η.

142x107mm (300 x 300 DPI)

This paper presented here as accepted for publication in Geophysics prior to copyediting and composition.
© 2020 Society of Exploration Geophysicists.

Downloaded 02/12/20 to 109.171.137.210. Redistribution subject to SEG license or copyright; see Terms of Use at http://library.seg.org/

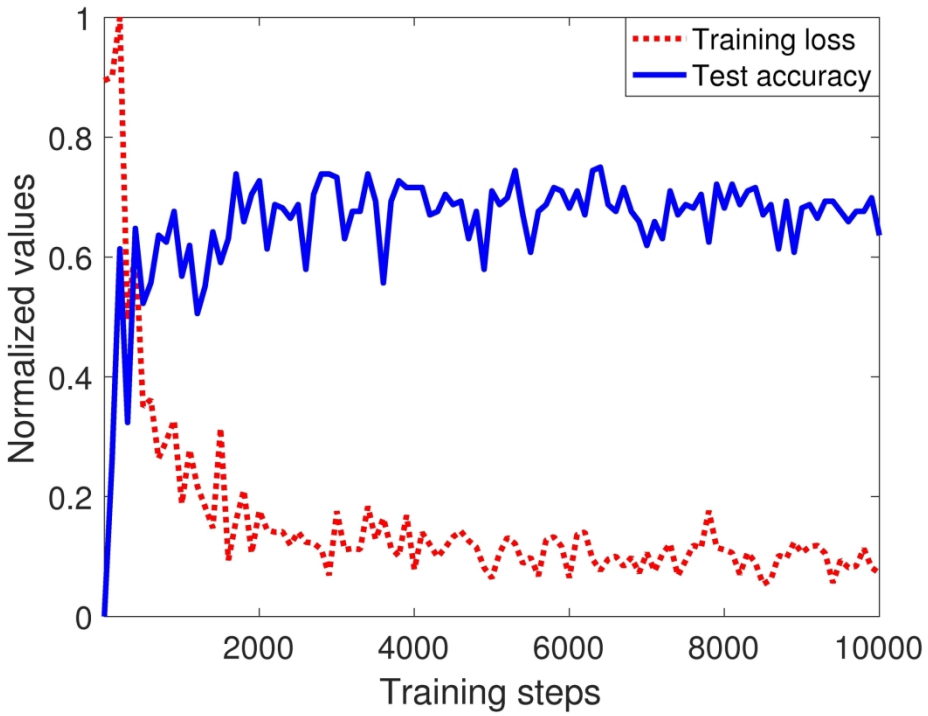

Figure8: Normalized training loss at every 100 steps. A total of 90% training loss is achieved with a random dropout of 10% for each layer, while the validation accuracy stays around 70%.

197x148mm (300 x 300 DPI)

This paper presented here as accepted for publication in Geophysics prior to copyediting and composition.
© 2020 Society of Exploration Geophysicists.

Downloaded 02/12/20 to 109.171.137.210. Redistribution subject to SEG license or copyright; see Terms of Use at http://library.seg.org/

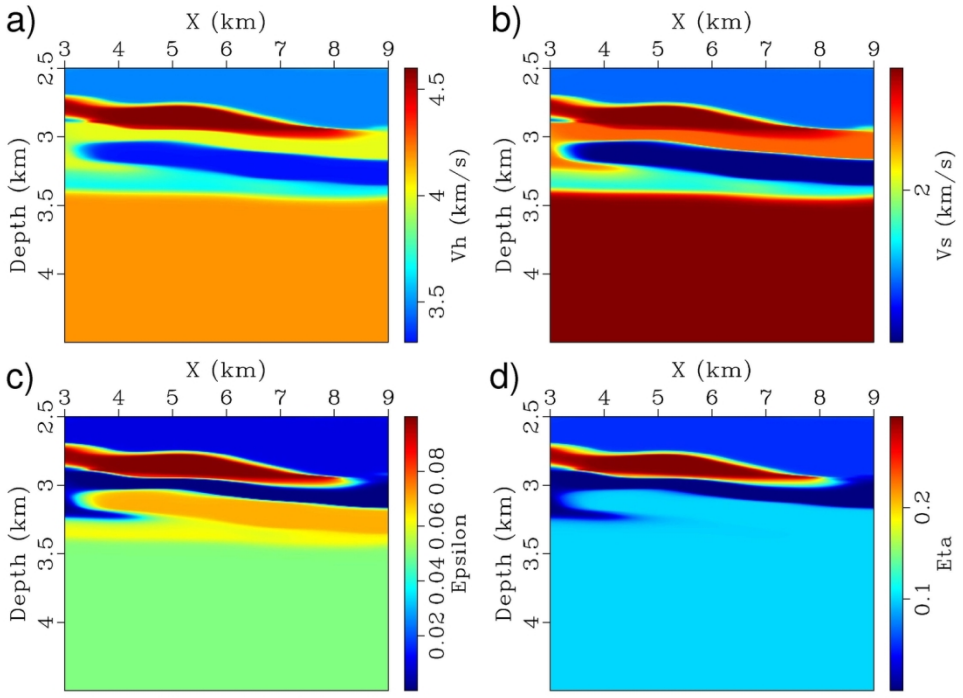

Figure9: The predicted facies distribution after training. They are converted to the parameters of a) v_h, b) v_s, c) ϵ and d) η. The number of colors is not equal to the number of faceis since the weighted summation can generate more parameter values in between and also different faceis can have the same value for certain parameters.

142x104mm (300 x 300 DPI)

This paper presented here as accepted for publication in Geophysics prior to copyediting and composition.
© 2020 Society of Exploration Geophysicists.

Downloaded 02/12/20 to 109.171.137.210. Redistribution subject to SEG license or copyright; see Terms of Use at http://library.seg.org/

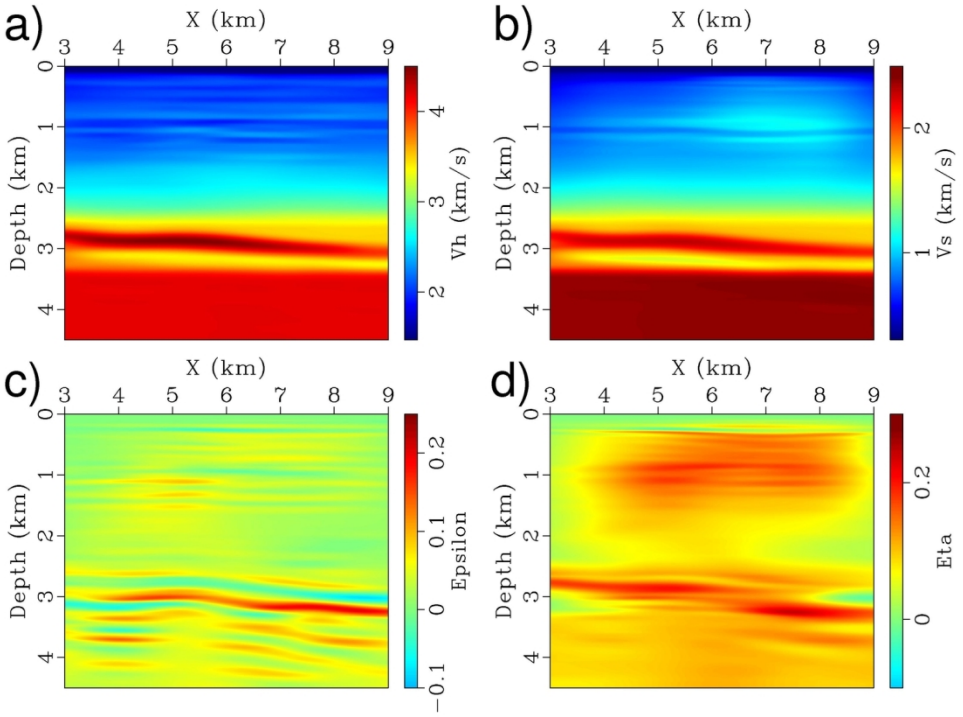

Figure10: The inverted models using the anisotropic elastic FWI with facies constraints. a) v_h, b) v_s, c) ϵ and d) η.

142x107mm (300 x 300 DPI)

This paper presented here as accepted for publication in Geophysics prior to copyediting and composition.
© 2020 Society of Exploration Geophysicists.

Downloaded 02/12/20 to 109.171.137.210. Redistribution subject to SEG license or copyright; see Terms of Use at http://library.seg.org/

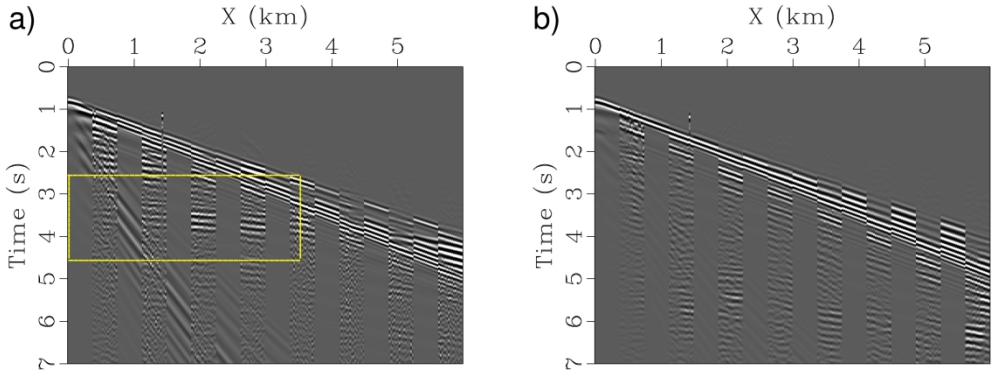

Figure11: A shot gather displaying interleaved predicted and observed data using the initial v_p and v_s as shown in Figure \ref{fig5}. a) Vertical and b) horizontal components. The dashed rectangular indicates the zoomed-in view plotted in Figure \ref{fig15}.

328x124mm (300 x 300 DPI)

This paper presented here as accepted for publication in Geophysics prior to copyediting and composition.
© 2020 Society of Exploration Geophysicists.

Downloaded 02/12/20 to 109.171.137.210. Redistribution subject to SEG license or copyright; see Terms of Use at http://library.seg.org/

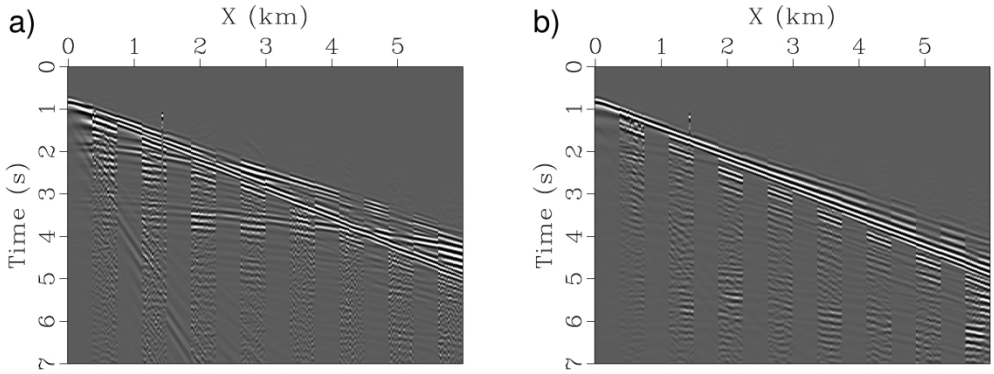

Figure12: A shot gather displaying interleaved predicted and observed data using the estimated v_p and v_s from isotropic inversion as shown in Figure \ref{fig6}. a) Vertical and b) horizontal components.

328x124mm (300 x 300 DPI)

This paper presented here as accepted for publication in Geophysics prior to copyediting and composition.
© 2020 Society of Exploration Geophysicists.

Downloaded 02/12/20 to 109.171.137.210. Redistribution subject to SEG license or copyright; see Terms of Use at http://library.seg.org/

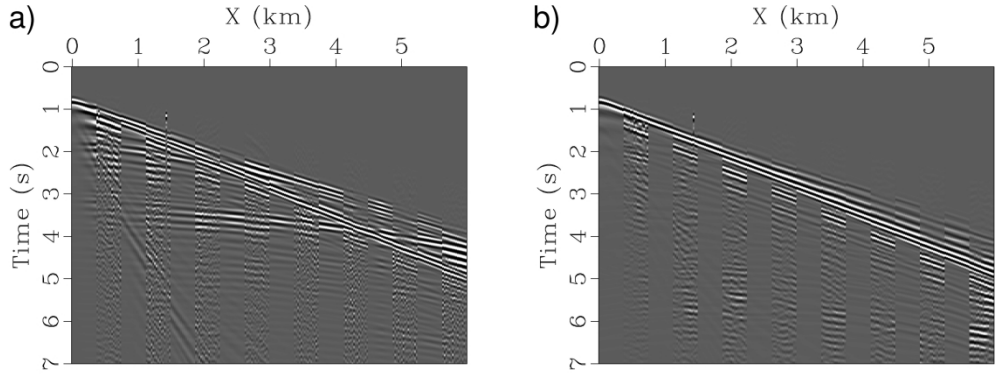

Figure13: A shot gather displaying interleaved predicted and observed data using the estimated v_h, v_s, ϵ and η from hierarchic VTI inversion as shown in Figure \ref{fig7}. a) Vertical and b) horizontal components.

328x124mm (300 x 300 DPI)

This paper presented here as accepted for publication in Geophysics prior to copyediting and composition.
© 2020 Society of Exploration Geophysicists.

Downloaded 02/12/20 to 109.171.137.210. Redistribution subject to SEG license or copyright; see Terms of Use at http://library.seg.org/

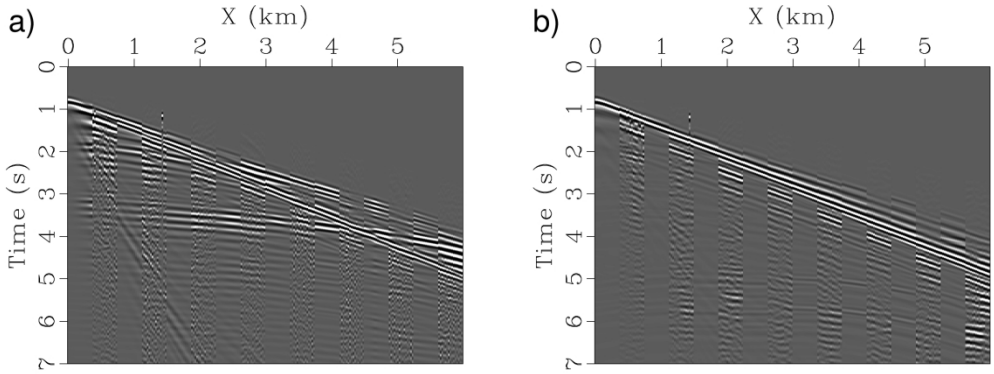

Figure14: A shot gather displaying interleaved predicted and observed data using the deep learning aided VTI inversion as shown in Figure \ref{fig10}. The matching of reflections of the vertical component are improved compared to the hierarchical VTI inversion (Figure \ref{fig13}). a) Vertical and b) horizontal components.

328x124mm (300 x 300 DPI)

This paper presented here as accepted for publication in Geophysics prior to copyediting and composition.
© 2020 Society of Exploration Geophysicists.

Downloaded 02/12/20 to 109.171.137.210. Redistribution subject to SEG license or copyright; see Terms of Use at http://library.seg.org/

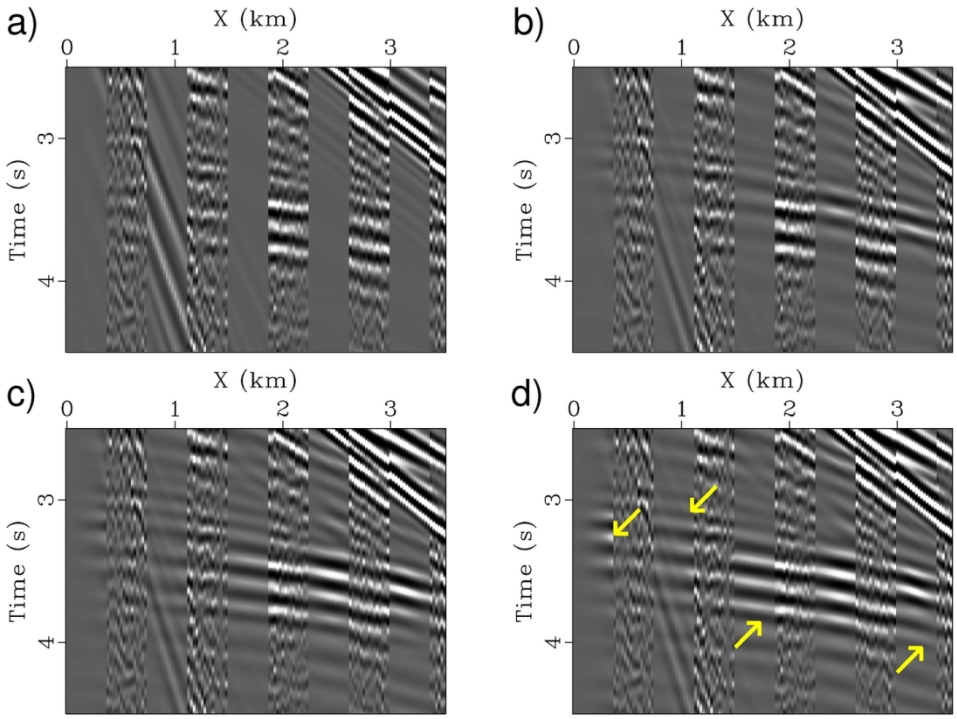

Figure15: A zoomed-in view of the vertical-component of the shot gathers. a), b), c) and d) are corresponding to the marked areas in Figures \ref{fig12}, \ref{fig13}, \ref{fig14} and \ref{fig16}, respectively. The arrows mark the improved phase matching.

136x104mm (300 x 300 DPI)

This paper presented here as accepted for publication in Geophysics prior to copyediting and composition.
© 2020 Society of Exploration Geophysicists.

Downloaded 02/12/20 to 109.171.137.210. Redistribution subject to SEG license or copyright; see Terms of Use at http://library.seg.org/

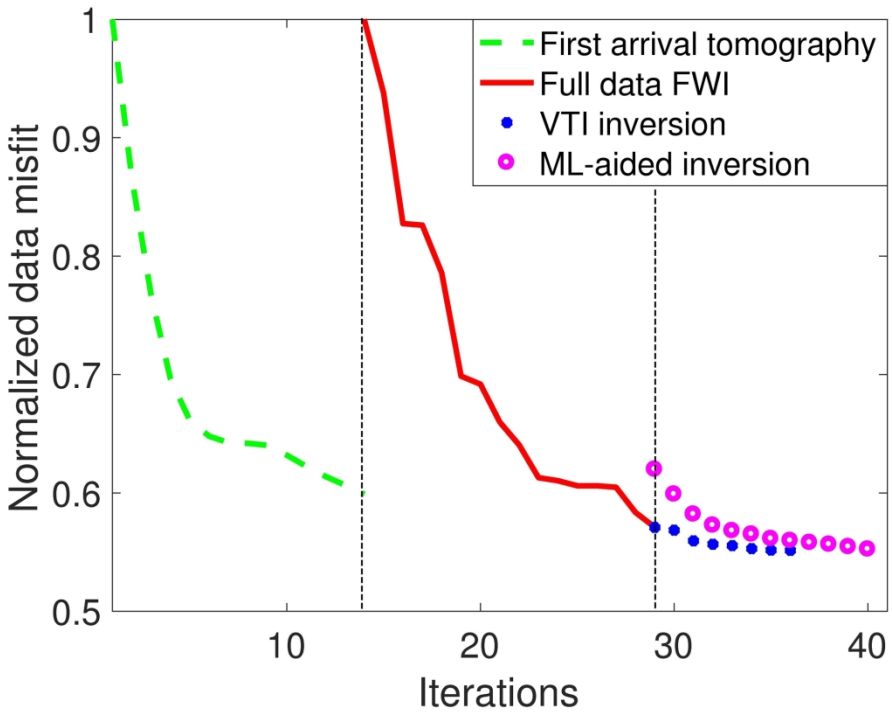

Figure16: Data matching history. There are three sequential inversions: 1) isotropic first arrival FWI, 2) isotropic full data FWI and 3) VTI inversions. The VTI inversions are parallel inversions: one is the hierarchical VTI inversion and another one is the proposed machine-learning aided inversion. The isotropic inversion reduces the data misfit by 40% and the follow-up deep learning aided inversion can further reduce the data misfit by about an additional 5%.

197x148mm (300 x 300 DPI)

This paper presented here as accepted for publication in Geophysics prior to copyediting and composition.
© 2020 Society of Exploration Geophysicists.

Downloaded 02/12/20 to 109.171.137.210. Redistribution subject to SEG license or copyright; see Terms of Use at http://library.seg.org/

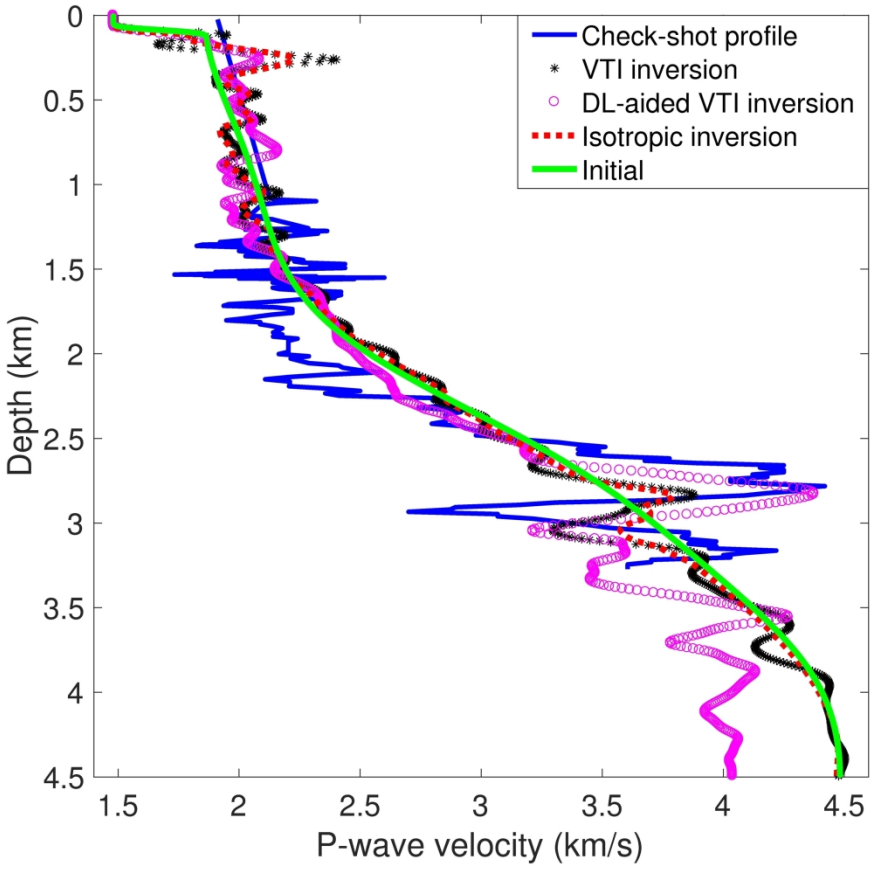

Figure17: Vertical P-wave velocity profiles at X=5.25 km.

236x220mm (300 x 300 DPI)

This paper presented here as accepted for publication in Geophysics prior to copyediting and composition.
© 2020 Society of Exploration Geophysicists.

Downloaded 02/12/20 to 109.171.137.210. Redistribution subject to SEG license or copyright; see Terms of Use at http://library.seg.org/

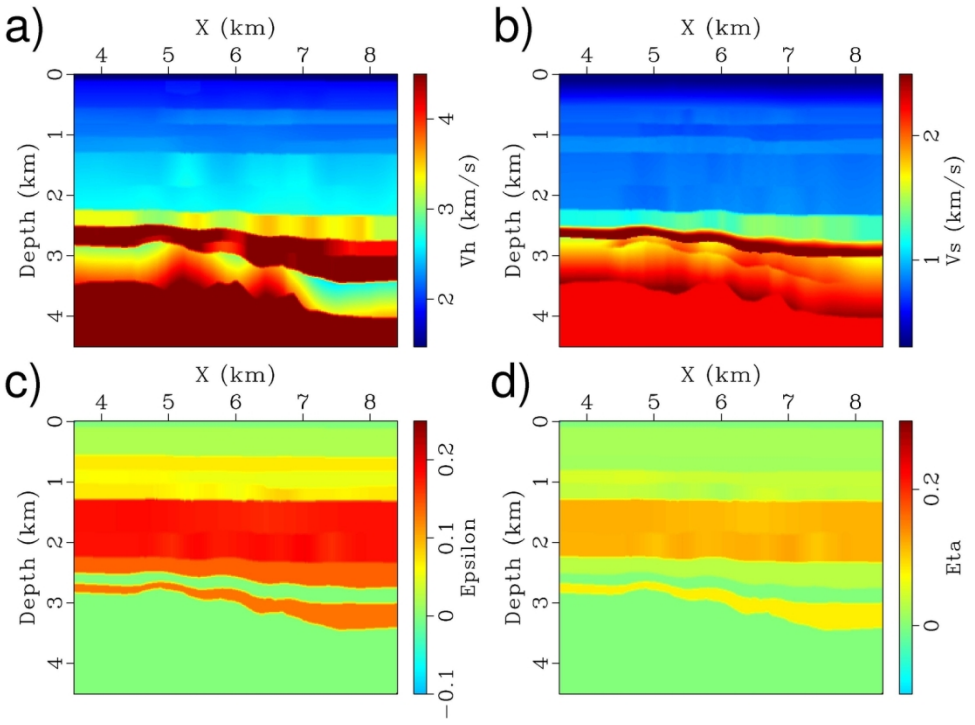

Figure18: The reference VTI model. a) v_h, b) v_s, c) ϵ and d) η, obtained using the layer-stripping tomography technique.

142x107mm (300 x 300 DPI)

This paper presented here as accepted for publication in Geophysics prior to copyediting and composition.
© 2020 Society of Exploration Geophysicists.

Downloaded 02/12/20 to 109.171.137.210. Redistribution subject to SEG license or copyright; see Terms of Use at http://library.seg.org/

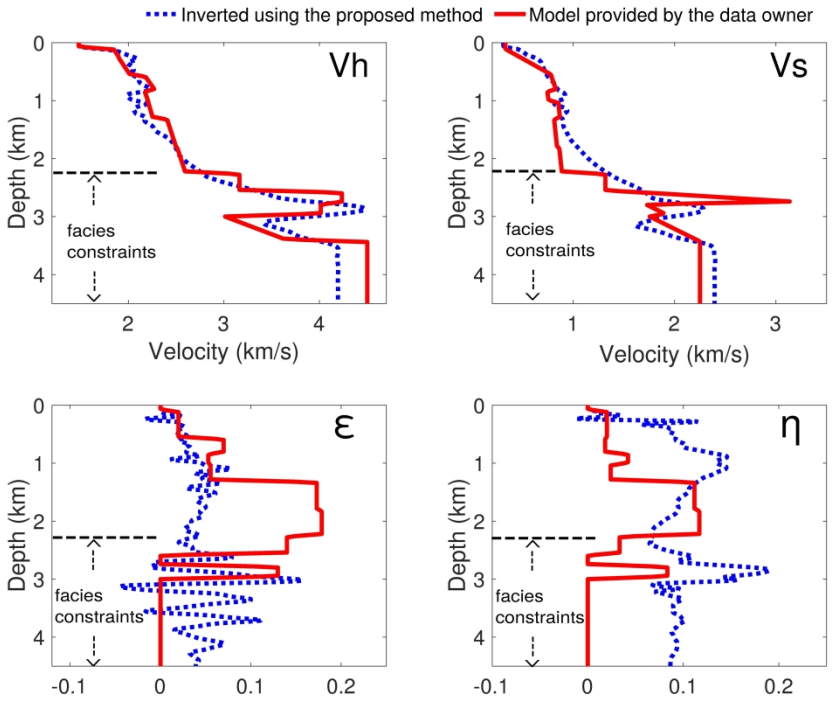

Figure19: A vertical-profile comparison of the parameters in terms of v_h, v_s, ϵ and η between the proposed inversion and the provided reference model at location X=5.25 km. The facies constraint is only applied below 2.3 km due to the availability of well log data.

336x257mm (300 x 300 DPI)

This paper presented here as accepted for publication in Geophysics prior to copyediting and composition.
© 2020 Society of Exploration Geophysicists.

DATA AND MATERIALS AVAILABILITY

Data associated with this research are available and can be accessed via the following URL:lt;brgt; Note: A digital object identifier (DOI) linking to the data in a general or discipline-specific data repository is strongly preferred.

Downloaded 02/12/20 to 109.171.137.210. Redistribution subject to SEG license or copyright; see Terms of Use at http://library.seg.org/

This paper presented here as accepted for publication in Geophysics prior to copyediting and composition.
© 2020 Society of Exploration Geophysicists.